Optik 158 (2018) 522–534

Contents lists available at ScienceDirect

Optik

journal homepage: www.elsevier.de/ijleo

Original research article

Improving the photovoltaic performance of DSSCs using a combination of mixed-phase TiO_2 nanostructure photoanode and agglomerated free reduced graphene oxide counter electrode assisted with hyperbranched surfactant

A.B. Suriani[a,b,*], Muqoyyanah[a,b], A. Mohamed[a,c], M.H. Mamat[d], N. Hashim[a,c], I.M. Isa[a,c], M.F. Malek[d,e], M.I. Kairi[f], A.R. Mohamed[f], M.K. Ahmad[g]

[a] *Nanotechnology Research Centre, Faculty of Science and Mathematics, Universiti Pendidikan Sultan Idris, 35900, Tanjung Malim, Perak, Malaysia*
[b] *Department of Physics, Faculty of Science and Mathematics, Universiti Pendidikan Sultan Idris, 35900, Tanjung Malim, Perak, Malaysia*
[c] *Department of Chemistry, Faculty of Science and Mathematics, Universiti Pendidikan Sultan Idris, 35900, Tanjung Malim, Perak, Malaysia*
[d] *NANO-ElecTronic Centre (NET), Faculty of Electrical Engineering, Universiti Teknologi MARA (UiTM), 40450 Shah Alam, Selangor, Malaysia*
[e] *NANO-SciTech Centre (NST), Institute of Science (IOS), Universiti Teknologi MARA (UiTM), 40450 Shah Alam, Selangor, Malaysia*
[f] *School of Chemical Engineering, Engineering Campus, Universiti Sains Malaysia, Nibong Tebal, Seberang Perai Selatan, Pulau Pinang, Malaysia*
[g] *Microelectronic and NanotechnologyShamsuddin Research Centre (MiNT-SRC), Faculty of Electrical and Electronic Engineering, Universiti Tun Hussein Onn Malaysia, 86400, Parit Raja, Batu Pahat, Johor, Malaysia*

ARTICLE INFO

Article history:
Received 29 November 2017
Accepted 28 December 2017

Keywords:
Reduced graphene oxide
Hyperbranched surfactant
Mixed-phase TiO_2
Nanostructures
Efficiency
DSSCs

ABSTRACT

The role of hyperbranched surfactant, namely, sodium 1,4-bis (neopentyloxy)-3-(neopentyloxycarbonyl)-1,4-dioxobutane-2-sulphonate (TC14), in the synthesis and stabilisation of reduced graphene oxide (rGO) as counter electrode (CE) thin film was investigated for dye-sensitised solar cell (DSSCs) application. The energy conversion efficiency (η) of CE-based rGO from TC14 (TC14-rGO) was 0.0266%, with a short current density, open circuit voltage and fill factor of 0.222 mA/cm^2, 0.697 V and 14.15, respectively. The efficiency of the surfactant was two times higher than that of CE-based rGO from single-tail sodium dodecyl sulphate surfactant. Graphene oxide (GO) was initially synthesised by electrochemical exfoliation method. Hydrazine hydrate was subsequently used in the production of rGO through chemical reduction process. Spraying deposition method was used to transfer GO and rGO solutions and fabricate GO and rGO CE thin films. A novel combination of hydrothermal growth and squeegee method in the synthesis and production of mixed-phase titanium dioxide (TiO_2) nanostructures as photoanode was selected due to its simple and low-cost method. Rutile TiO_2 nanorods and anatase TiO_2 nanoparticles are essential in electron transfer process and dye adsorption, respectively. Therefore, these combinations resulted in improved photocatalytic activity and η of dye-sensitised solar cells when TC14-rGO was used.

* Corresponding author at: Nanotechnology Research Centre, Faculty of Science and Mathematics, Universiti Pendidikan Sultan Idris, 35900, Tanjung Malim, Perak, Malaysia.
E-mail address: absuriani@yahoo.com (A.B. Suriani).

https://doi.org/10.1016/j.ijleo.2017.12.149
0030-4026/

1. Introduction

The dependency on coal, oil and gas for electricity can be reduced by utilising solar energy, including the fabrication of dye-sensitised solar cells (DSSCs). DSSCs become a remarkable and promising subject since its invention by O'Regan and Grätzel in 1991 [1] to replace silicon-based solar cells due to its simple fabrication, inexpensive nature, light weight and high energy conversion efficiency (η) [2]. Although approximately 13% efficiency was achieved by Mathew et al. [3], the improvement of DSSCs performance, such as the improvement of photoanode and counter electrode (CE) and the replacement of dye or electrolyte, remains unexplored.

Platinum (Pt) has been widely used as a CE, which is important in DSSCs performance to facilitate electron transfer [4–6]. Unfortunately, the high cost due to Pt scarcity limits its application. The development of new electrode materials with high transparency, low cost and high conductivity has become an important issue in Pt replacement [7]. Graphene, a new 2D carbon nanomaterial composed of sp^2 carbon arranged in a honeycomb lattice, becomes a promising alternative for Pt [8–10] because of its excellent electrical and optical properties [11–14]. Chemical vapour deposition is the most popular method to yield high purity and controllable thickness of produced graphene. Unfortunately, this method involves an explosive precursor with high synthesis temperature of approximately 1000 °C [15]. Graphene oxide (GO), as a graphene derivative, is an alternative approach; this compound can be chemically synthesised on the basis of Hummers' method. High-quality GO is also produced by using this method, but strong acids and other hazardous chemicals are utilised. Moreover, the complex synthesis steps limit the application of this method [16]. The transfer process to fabricate thin film is also a challenge due to the powder form of produced graphene and GO based on both methods. A dispersing agent, such as tetrahydrofuran [17], carbonated water [18] and dimethylformamide (DMF) [19], is required to disperse GO powder into the solution form, thereby making it easily transferrable. Electrochemical exfoliation, a simple and low-cost method, can be a promising method to produce GO in the solution form, which can be easily transferred into a desired substrate. Furthermore, electrochemical exfoliation offers a considerable potential in large-scale production due to the high volume of produced solution from a single-synthesis process [20].

Solvents used as electrolytes in the electrochemical process include acetonitrile, DMF, dimethylsulfoxide, propylene carbonate, nitric acid and sulfuric acid [21,22]. Water-based exfoliation, which utilises surfactants, offers a more environment-friendly approach than that of chemical, acid or sulfuric electrolytes. The hydrophobic nature of surfactant chains attached to the carbon bonds and hydrophilic heads of the surfactant stabilise the graphene dispersion in the solution. Therefore, the surfactant chain number is important in the exfoliation process because it determines the quality of synthesised GO. The intercalation process during electrochemical exfoliation can be increased by increasing the number of surfactant tail groups. Mohamed et al. [23–25] investigated the single-, double- and triple-tail surfactants and showed that the triple-tail customised surfactant, namely, sodium 1,4-bis (neopentyloxy)-3-(neopentyloxycarbonyl)-1,4-dioxobutane-2-sulphonate (TC14), improves the multiwalled carbon nanotube dispersion in latex nanocomposites. Additionally, different surfactant tail groups in one-step electrochemical exfoliation intermixed with natural rubber latex (NRL) nanocomposite are successfully utilised in previous work [26]. The fabricated electrode utilising TC14 surfactant also yields higher conductivity and capacitance value than that of the commercially available single-tail sodium dodecyl sulphate (SDS) surfactant used in supercapacitor application. The high interaction of GO/NRL due to the triple interactions of TC14 surfactant results in wrinkled and crumpled tissue-like sheets with low agglomeration [27]. The further reduction process of the synthesised GO assisted with hyperbranched TC14 surfactant and subsequently mixed with the radiation vulcanisation NRL provides higher conductivity and capacitance values than those of the pure GO [28].

In the present work, both customised and commercially available surfactants were used in the water-based electrolyte preparation to assist the exfoliation process and investigate their effects on GO production. Chemical reduction process was carried out to produce reduced GO (rGO) due to a water-based solution that requires low temperature during reduction. Among several reducing agents, such as chemicals, plant extracts, microorganisms, proteins and hormones, hydrazine hydrate was selected due to its effectiveness in thin and fine rGO production [29]. The spraying deposition method was chosen among various transfer methods, such as chemical etching, roll-to-roll process, drop casting and spin and dip coating, to transfer GO and rGO solutions. This method was used due to its simple process, easy control, potential for large-scale production and suitability for various substrates [30]. Fluorine-doped tin oxide (FTO) was selected as a substrate with better performance than that of indium-doped tin oxide (ITO). ITO displayed thermal instability and a sheet resistance that was two times higher than that of FTO. A high η was achieved by using FTO; thus, this electrode is recommended for DSSCs application [31,32].

Several semiconductor oxide layers that have been used as photoanodes for DSSCs are ZnO [33], SnO_2 [9,10,34], Zn_2SnO_4 [35], $SrTiO_3$ [36] and TiO_2 [37–41]. TiO_2 becomes the most investigated and applied semiconductor oxide as a DSSCs photoanode semiconductor layer compared with those of ZnO and SnO_2 [42–44] due to its good properties, which include nontoxicity, low cost, good electronic properties, chemical and physical stabilities and large surface area [2,45–47]. The morphology of TiO_2 that is successfully synthesised to date includes nanoparticles [39], nanorods, nanoflowers [37,38], nanowires [48], nanotubes, nanocorals, yolk-shell, microspheres and hollow hemispheres [49–51]. TiO_2 nanoparticles are widely used semiconductor layers, which are utilised as photoanodes for DSSCs. Other types and modification of TiO_2 were investigated to achieve high η; these investigations include varying layer numbers [52], addition of different haze [53] and other metal oxide coatings [54], utilisation of other nanostructures and mixing the TiO_2 phase [55,56]. Combination of the crystallinity phase may yield high photocatalytic activity and consequently improve the η value.

In the present work, rutile–anatase mixed-phase TiO_2 nanostructures were synthesised to increase the dye adsorption, thereby increasing the photocatalytic activity in the DSSCs performance. The rutile phase of TiO_2 was limited and focused only on nanorods and nanoflowers, and nanoparticles were used for anatase phase. Hydrothermal growth and squeegee method were selected in the synthesis and production of rutile and anatase TiO_2 due to their simplicity and low cost [37–39]. In addition to the novel method used to produce CE thin films and photoanodes, this study uses customised hyperbranched surfactant to improve the rGO CE film dispersion compared with that of SDS-assisted rGO film and utilised mixed-phase TiO_2 using these methods. To the best of our knowledge, this paper is the first to report on DSSCs application that utilises mixed-phase TiO_2 photoanode combined with TC14-rGO CE film.

2. Experimental details

2.1. Chemicals

The customised TC14, a commercially available SDS (Sigma-Aldrich) surfactant, and graphite rods (99.99%, 150 mm length and 10 mm diameter, GoodFellow GmbH, Germany) were used in GO synthesis. Hydrazine hydrate (Merck, 80% soluble in water) was used as reducing agent in the rGO production. Titanium butoxide (TBOT) (Sigma-Aldrich), titanium (IV) isopropoxide (TTIP) (Sigma-Aldrich), titanium (IV) oxide (≥ 99.5%) (Sigma-Aldrich), hydrochloric acid (HCl, 36.5%–38% concentration) (JT Baker) and ethanol (95%, Systerm) were used for TiO_2 nanostructure synthesis. FTO (Vonke Co., Ltd., $\rho = 15\,\Omega/sq$) was used as substrate for both CE and photoanode films. Ditetrabutylammonium *cis*-bis(isothiocyanato)bis (2,2′-bipyridyl-4,4′-dicarboxylato)ruthenium(II) (N719) (Sigma-Aldrich), acetonitrile (QRëC) and 1-butanol (Laboratory Chemicals) were used for dye solution. Veloron nitrile (Sigma-Aldrich), 4-*tert*-butylpyridine (Sigma-Aldrich), iodolyte (Solaronix), dimethyl-propyl-benzimidiazole iodide (DMPII) (Solaronix) and guanidine thiocyanate (QRëC) were used in electrolyte preparation.

2.2. Fabrication of GO and rGO CE thin films

Two different ionic surfactants, namely, TC14 and SDS, are customised and commercially available, respectively. These surfactants were used in the GO synthesis using electrochemical exfoliation method. Two graphite rods were partially immersed in the prepared electrolyte (0.1 M) and connected to 7 V DC power supply for 24 h synthesis time. Afterwards, the rGO was chemically reduced by hydrazine hydrate at a GO solution-to-hydrazine hydrate ratio of 100:1. The reduction process was carried out under constant stirring and a maintained temperature of ∼95 °C for 24 h. The produced GO and rGO were transferred by spraying deposition method onto preheated cleaned FTO substrate (2×1 cm^2) at 120 °C. The spraying process was conducted using an airbrush with 0.3 mm nozzle diameter placed at a 10 cm distance from the substrate. Annealing process at 400 °C was further performed in ambient argon for 1 h.

2.3. Fabrication of mixed-phase TiO_2 nanostructures as photoanodes

The rutile TiO_2 nanorods–nanoflowers film as a photoanode bottom layer was synthesised using hydrothermal growth [38]. Approximately 120 ml of both hydrochloric acid and deionised (DI) water (1:1/V) was stirred for 5 min prior to the dropwise addition of 3 ml of TBOT into the solution. The solution was stirred for another 10 min. The prepared hydrothermal solution was transferred into an autoclave that was previously used with FTO substrates with the conductive surface facing upward. The hydrothermal growth process was conducted at 150 °C for 5 h. The samples were removed when the autoclave was cooled down to room temperature. Subsequently, the samples were rinsed using DI water and dried at room temperature. The anatase TiO_2 nanoparticles as a second layer of photoanode were fabricated using squeegee method [39]. The TiO_2 paste was initially prepared by mixing titanium (IV) oxide and ethanol and adding TTIP under manual stirring, until a low-agglomeration paste was formed. The paste was sonicated for 5 min before applying it onto TiO_2 nanorods–nanoflowers film. The mixed-phase TiO_2 film was heated in an electric oven at 150 °C for 10 min and annealed at 450 °C for 1 h in a furnace.

2.4. Fabrication of DSSCs

N719 (0.3 mM) was used as a dye for 24 h of photoanode immersion. The dyed photoanode films were initially rinsed with ethanol to remove the residues before assembly with GO and rGO CE thin films. The DMPII electrolyte that contains redox couple was dropped through the space between the assembled films. The assembled film was connected to solar simulator devices to investigate its performance.

2.5. Characterisation techniques

The morphology of fabricated photoanodes and CE thin films with the element compound were determined using FESEM-Hitachi SU8020 and EDX-Horiba EMAX. The HRTEM-JEOL JEM 2100, XRD-Bruker D8 Advance and micro-Raman spectroscopy (Renishaw InVia microRaman System) were used to determine the crystallinity properties. Data analysis, including the phase, crystallite size and its percentage, was performed by Diffrac.eva V4.0 software on the basis of the XRD data. The integral (I) breadth, instead of FWHM, was used for crystallite size calculation due its remarkably accurate calculation. In addition,

the optical and electrical properties were determined using Agilent Technologies Cary 60 UV–vis. I–V characteristics were obtained by using four-point probe equipment with Keithley 2636A as sourcemeter and Leios TMXpert software for data analysis. The DSSCs efficiency was measured using solar simulator Oriel Sol 1A under AM 1 solar illumination.

3. Results and discussion

Fig. 1(a) illustrates the fabricated photoanode film that comprises two TiO_2 nanostructures layers, namely, nanorods–nanoflowers at the bottom part and nanoparticles at the upper layers. A dense and uniform tetragonal crystal structure of TiO_2 nanorods with a diameter range of 99.2–310 nm was successfully grown on the entire FTO substrate (Fig. 1(b) and (c)). A large TiO_2 nanoflower (8.17 μm diameter), which is similar to a chrysanthemum, was also observed on top of the TiO_2 nanorods (Fig. 1(d)). The diameter of tetragonal TiO_2 nanoflower structure varied from 146 nm to 476 nm, which was ~1.5 times larger than that of TiO_2 nanorod diameter

(Fig. 1(e)). The large size of TiO_2 nanoflowers may be due to the high amount of Ti^{4+} ions in the solution, which resulted from the slow hydrolysis rate caused by the high acidity of the solution. The abundant Ti^{4+} ions fall and form the petals of the TiO_2 nanoflowers on the remaining crystal nucleus with different crystal faces that are stacked on top of TiO_2 nanorods [57]. The TiO_2 nanoflower growth was evenly scattered on top of TiO_2 nanorods with an evident distance from one another, thereby making them unobservable in FESEM images at 5 K magnification.

The surface morphology of TiO_2 nanoparticles applied on top of TiO_2 nanorods–nanoflowers is shown in Fig. 1(f). FESEM images indicated that TiO_2 nanoparticles completely and uniformly covered the nanorods with minimal cracking. The average

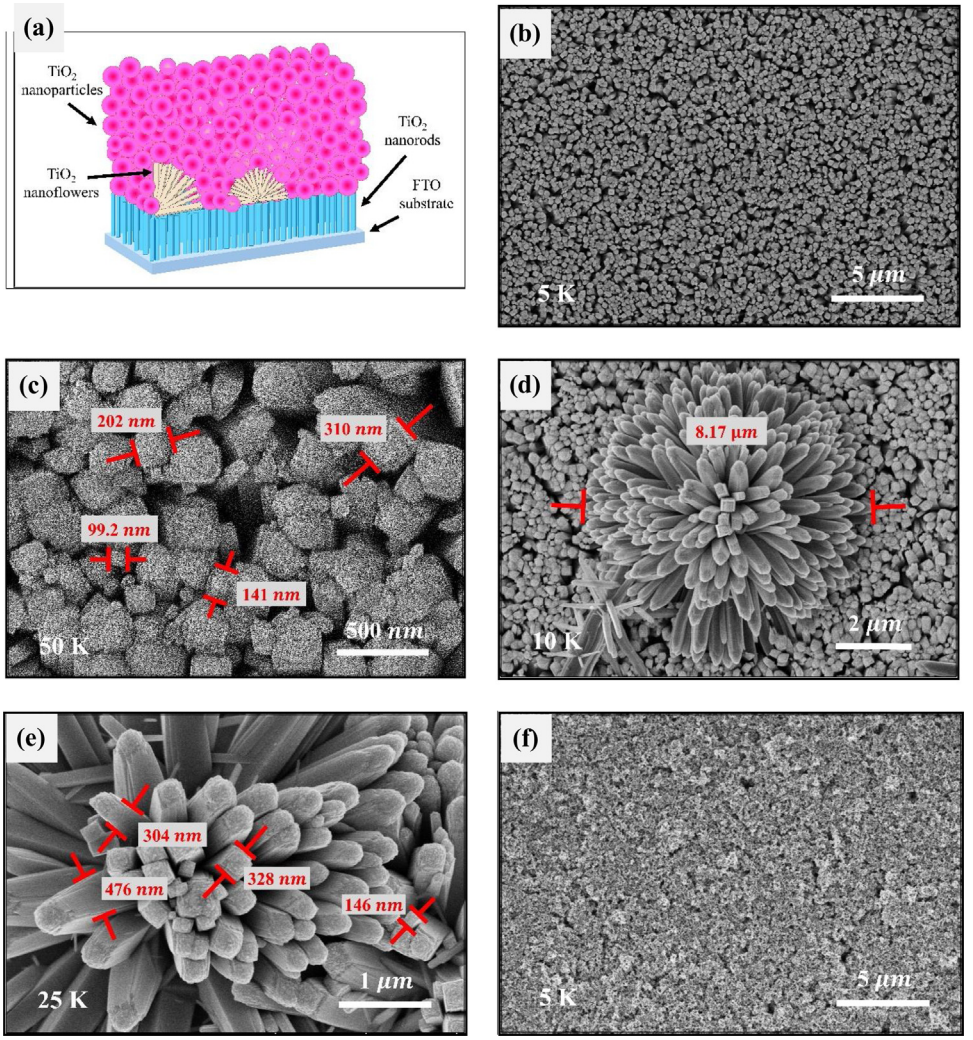

Fig. 1. (a) Illustration of fabricated photoanode. FESEM images of the (b) top view and (c) diameter of rutile TiO_2 nanorods, (d) top view and (e) diameter of rutile TiO_2 nanoflowers, (f) top view and (g) diameter of TiO_2 nanoparticles and (h) cross section of fabricated photoanode film. EDX analysis of (i) rutile TiO_2 nanorods–nanoflowers and (j) mixed-phase TiO_2 nanostructures.

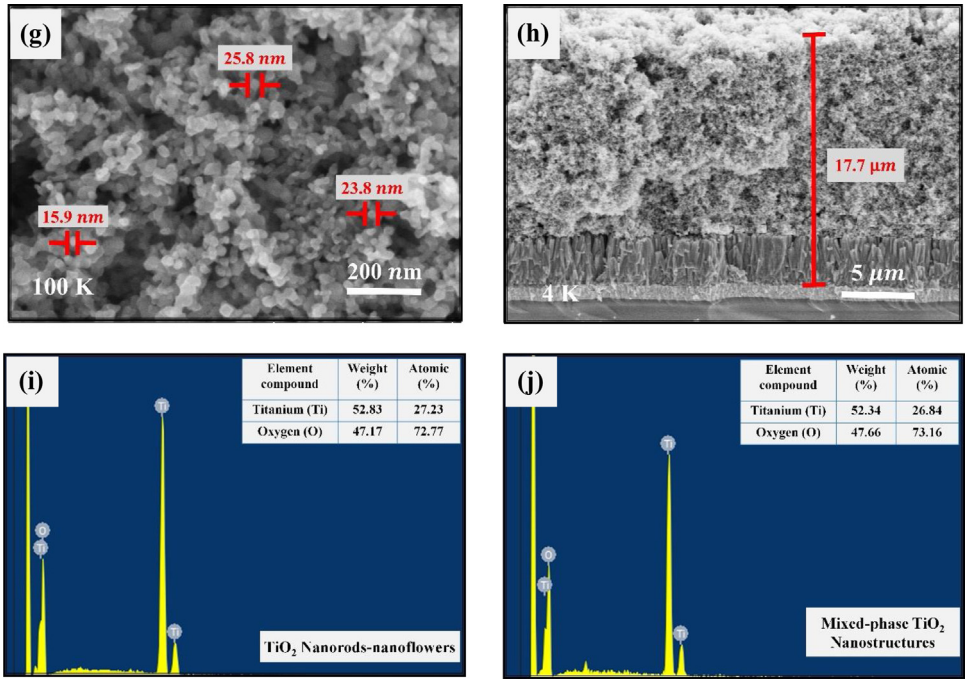

Fig. 1. *Continued*

diameter of synthesised TiO_2 nanoparticles varied from 15.9 nm to 25.8 nm (Fig. 1(g)). The nanocrystalline particles produced by TiO_2 paste were linked to one another due to the effective molar ratio of TTIP (0.1M) in the paste preparation. Low TTIP molarity results in fragile and collapsed film, whereas high molarity makes the film unstable because it can be easily peeled off from the substrate [39]. The interconnected nanoparticles showed high porosity, which is effective for dye adsorption, thereby increasing the photocurrent. The overall photoanode film thickness was 17 μm, as shown in Fig. 1((h)). High-density nanorods were clearly observed and grown perpendicularly on the FTO surface with an average length of 3.37 μm; this result is comparable to that of Ahmad et al. [38]. According to Fig. 1((h)), the TiO_2 nanoparticle thickness was in the range of 12.99–14.29 μm, which was ~76% of total photoanode film thickness. This thickness provided an advantage in terms of dye adsorption, which was supported by the high film porosity. Further EDX analysis (Fig. 1(i) and (j)) confirmed that Ti and O were the elemental compound of photoanode film. The Ti and O atomic percentages presented in the inset were ~27.23% and ~26.84%, respectively. Additionally, ~72.77% and ~73.16% are shown for rutile TiO_2 nanorods–nanoflowers and mixed-phase TiO_2 nanostructure films, respectively.

The GO and rGO thin-film morphologies determined by FESEM are presented in Fig. 2. The rGO thin film assisted with TC14 (TC14-rGO) exhibited the thinnest layer (Fig. 2(a)) compared with those of rGO thin film assisted with SDS (SDS-rGO) and GO thin film assisted with TC14 (TC14-GO) presented in Fig. 2(c) and (e). The thinnest layer of TC14-rGO is due to the triple interactions of TC14 surfactant, which causes the three-order distance between the graphite layers [23]. Moreover, the wrinkled and crumpled tissue-like morphology was evident for TC14-rGO layer, as shown by white arrows. This morphology was only slightly observed in SDS-rGO and TC14-GO films. The wrinkled structure prevented the layers from restacking, which confirmed the effective stabilisation role of TC14 surfactant. Many transparent fold-up layers in the edge plane, as shown by red arrows, were also evident for TC14-rGO. The thick layer and high GO agglomeration of SDS-rGO sample, as presented by yellow arrows, confirmed that the use of single-tail surfactant was less efficient to oxidise graphite. The thicker layer of TC14-GO than that of TC14-rGO may be due to the higher oxygen functional groups formed during oxidation. Hydrazine hydrate removed a part of oxygen functional groups during chemical reduction process, thereby forming a thin layer, as shown in the TC14-rGO film.

The EDX analysis shown in Fig. 2(b), (d) and (f) revealed C and O as GO and rGO thin film compounds. The spectra indicated that the reduction process was successful, as indicated by the decrease of O percentage from 81.98% (TC14-GO) to 33.34% (TC14-rGO). The SDS-rGO showed higher O percentage (48.83%) than that of TC14-rGO, which confirmed its thicker layers shown by FESEM images.

Given the customised and commercially available surfactants used to assist and fabricate GO and rGO films, HRTEM analysis was further conducted to determine the film layer number. Fig. 3(a) and (b) illustrate that the stacked layers were evident in SDS-rGO, which confirmed the thick layer (~3–5 layers) shown by FESEM images. The HRTEM image of TC14-GO (Fig. 3(c)) shows a thicker layer than that of SDS-rGO. This thick layer (~4–6 layers) of TC14-GO (Fig. 3(d)) may be due to the oxygen functional groups below and above GO layers [27]. After the chemical reduction process performed on TC14-GO,

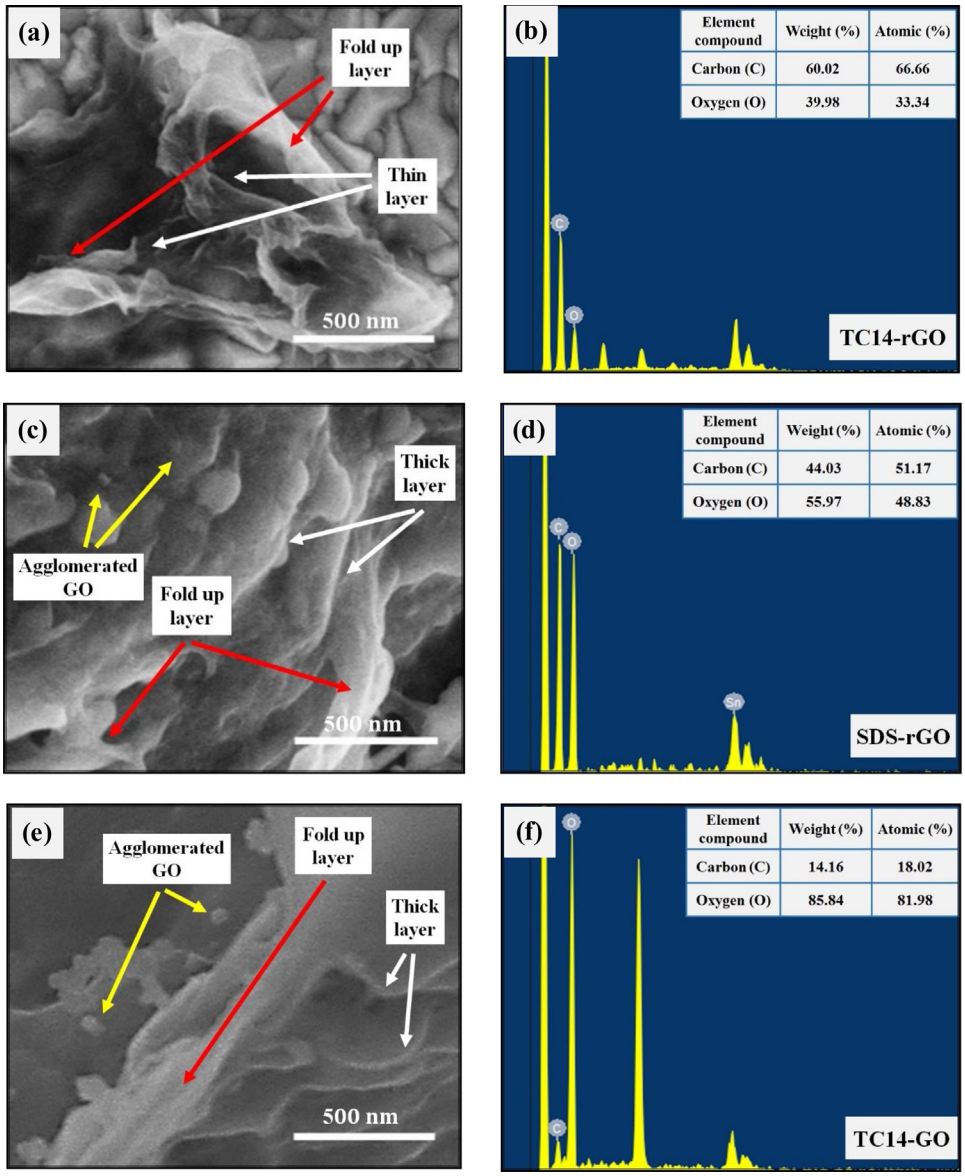

Fig. 2. FESEM images and EDX analysis of GO and rGO CE thin films: (a)–(b) TC14-rGO, (c) –(d) SDS-rGO and (e) –(f) TC14-GO.

the thin layers of TC14-rGO (~2–4 layers) were clearly observed; these layers indicated that hydrazine hydrate effectively removed the oxygen functional groups (Fig. 3(e) and (f)). The wrinkled structure of TC14-rGO helps electrolytes diffuse in DSSCs devices [58]. In addition, TC14-GO and TC14-rGO exhibited fold-up layers in the edge plane (shown by white arrows), which suggested the successful oxidation during electrochemical exfoliation. The interlayer spacing between two layers was ~0.35 nm, which is in accordance with that in theory.

Micro-Raman spectroscopy was carried out to investigate the crystallinity and defect density of photoanodes and CE films, respectively. The micro-Raman spectra of TiO_2 nanorods–nanoflowers revealed five peaks in the range of 100–800 cm^{-1}, as shown in Fig. 4(a). The weak sharp band observed at 119 cm^{-1} was related to B_{1g} mode, where the broad band caused by the disordered lattice centred at 238 cm^{-1} is related to multiple phonon scattering [37,59]. Additionally, the 238 cm^{-1} peak was associated with the nanometre scale of TiO_2 nanorods. Two intense peaks, which were representative of rutile characteristics, were evident at 446 (E_g) and 612 cm^{-1} (A_{1g}) [60]. The small bump observed at 694 cm^{-1} confirmed the formed nanorods–nanoflowers. Three Raman active modes based on three observed dominant peaks, expressed as $A_{1g} + B_{1g} + E_g$, confirmed that the synthesised film was in the rutile phase [37,61–64]. Four additional peaks were observed when TiO_2 nanoparticles were applied on top of TiO_2 nanorods–nanoflowers (Fig. 4(b)). The strongest peak at 144 cm^{-1} was related to the E_g mode in the anatase phase of TiO_2 nanoparticles. Other peaks related to the anatase phase were also observed at 198, 399 and 518 cm^{-1} [59,61,62]. After applying TiO_2 nanoparticles, three initial peaks of TiO_2 nanorods–nanoflowers at

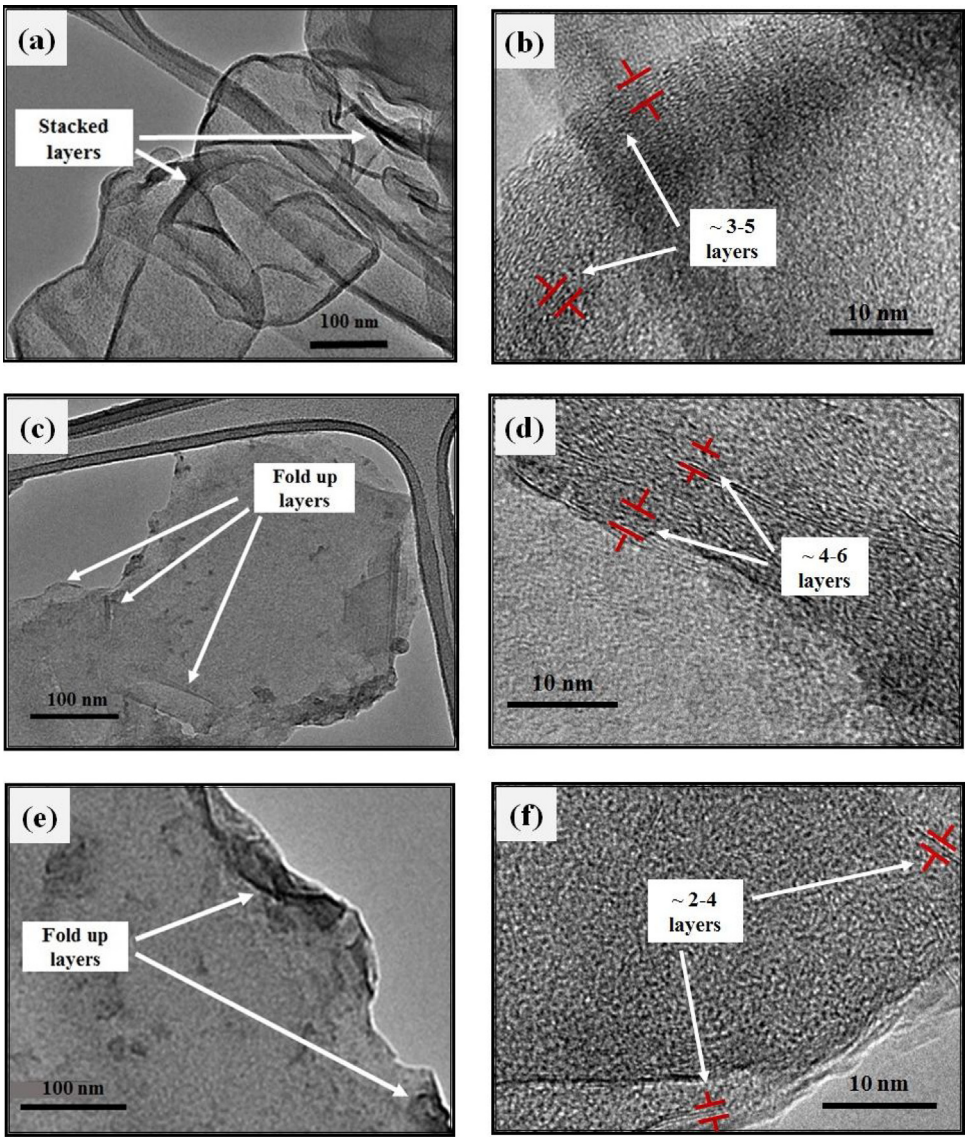

Fig. 3. HRTEM images of GO and rGO CE thin films: (a)–(b) SDS-rGO, (c)–(d) TC14-GO and (e)–(f) TC14-rGO.

Table 1
Raman band peak and intensity of graphene oxide (GO) and reduced GO (rGO) counter electrode (CE) thin films.

No.	CE thin films	D-peak (cm^{-1})	G-peak (cm^{-1})	2D-peak (cm^{-1})	I_D (a.u)	I_G (a.u)	I_{2D} (a.u)	I_D/I_G
a.	SDS-rGO	1378	1585	2723	250	427	278	0.59
b.	TC14-GO	1355	1585	2714	833	1608	1255	0.52
c.	TC14-rGO	1356	1586	2718	1494	2124	1564	0.70

119, 446 and 612 cm^{-1} shifted by ±1–2 cm^{-1} to 117, 448 and 611 cm^{-1}, respectively. The existence of TiO_2 nanoparticles influenced the peak location and the peak intensity of TiO_2 nanorods–nanoflowers. Two initial intense peaks intensity of TiO_2 nanorods–nanoflowers were decreases. This result confirmed that the fabricated film was in the mixed-phase of rutile–anatase.

Raman spectroscopy can characterise graphitic materials because considerable amount of information, including the graphene layer number, crystallinity, oxidation and defect level of the sample, can be obtained [65,66]. The micro-Raman spectra of GO and rGO CE thin films are presented in Fig. 4(c). Overall, all three samples showed the D-, G-, 2D- and G^+-band peaks in the range of 1200–2900 cm^{-1} with different shapes and intensities. The details of peak location and their intensity are presented in Table 1. The ratio of D-band intensity (I_D) to G-band intensity (I_G), known as I_D/I_G, can be used to estimate the sample crystallinity, including the defect number. The spectrum indicated that the TC14-GO showed the

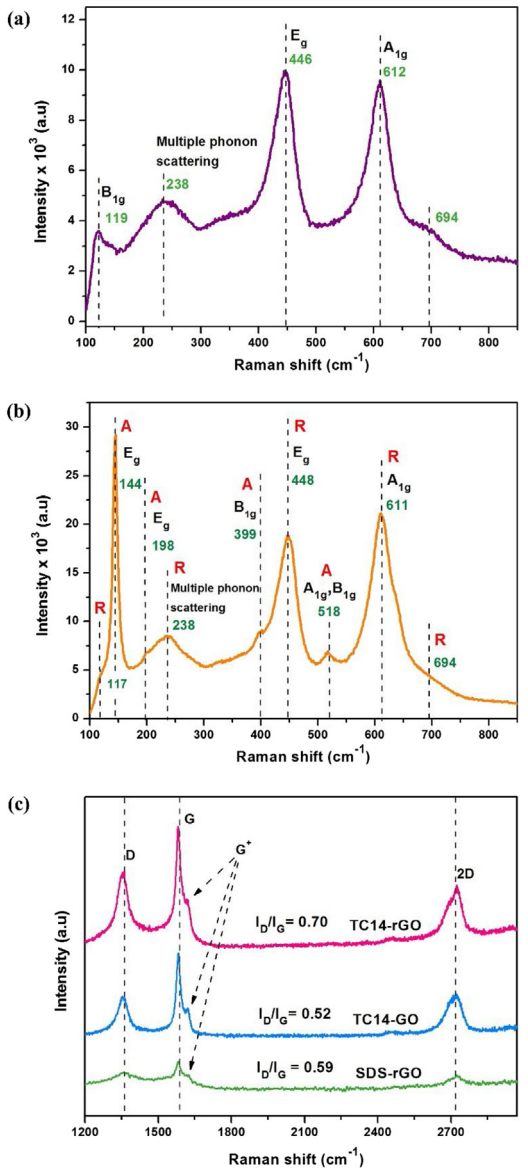

Fig. 4. Micro-Raman spectra of (a) rutile TiO_2 nanorod–nanoflower, (b) mixed-phase TiO_2 nanostructure and (c) GO and rGO CE thin films.

lowest I_D/I_G (0.52) compared with those of SDS-rGO (0.59) and TC14-rGO (0.70) samples. This result was possibly due to the high number of oxygen functional groups during electrochemical exfoliation. The successful chemical reduction process of TC14-GO utilising hydrazine hydrate was confirmed by the increased I_D/I_G of TC14-rGO. The highest I_D/I_G of TC14-rGO showed high crystallinity and defect level of the sample, which were evidenced with the wrinkles and crumpled tissue-like morphology shown in the FESEM images. The increased I_D/I_G also indicated the increase in sp^2 cluster number and newly formed graphitic domains with the decreased average size of sp^2 domain after the reduction process [29,67]. These results verified the low effectiveness of SDS surfactant, as shown by the low I_D/I_G of SDS-rGO after the reduction process.

The red-shifted G-band peak of the entire samples compared with that of graphite (1581.4 cm^{-1}) indicated the successful oxidation during electrochemical exfoliation. The additional peak (1619–1622 cm^{-1}), known as G^+-band, was also observed for the entire samples. This result suggested the high defect level at both basal and edge sites of the samples caused by the surfactant intercalation in the GO layers. The last peak, known as 2D-band (2714–2723 cm^{-1}), can be used to determine the layer number of the sample. According to the spectrum, the highest and sharpest 2D-band peaks were achieved by TC14-rGO, which confirmed the thinnest layers (~2–4 layers) shown in FESEM and HRTEM images. This result was also verified by the layer number calculation using the following equation: $\omega_G = 1581.6 + 11/(1 + n^{1.6})$. When the ω_G was replaced with the G-band position of TC14-rGO (1586 cm^{-1}), the calculated layer number of TC14-rGO was 1.95 [68].

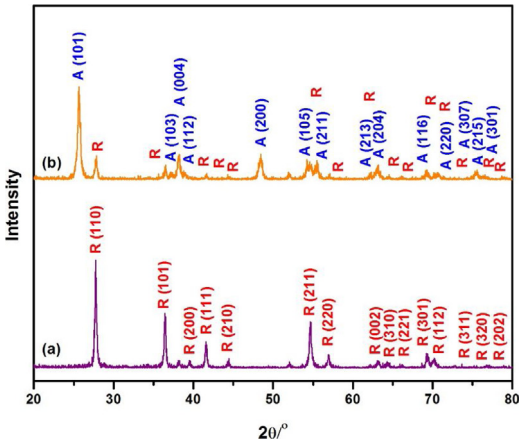

Fig. 5. XRD patterns of (a) rutile TiO_2 nanorods–nanoflowers and (b) mixed-phase TiO_2 nanostructures.

Table 2
Crystallite size and its percentage of the selected peaks of fabricated photoanode film (A, anatase; R, rutile).

No.	TiO_2 films	Peak (°)	Crystallite size (nm)	Crystallite percentage (%)
a.	TiO_2 nanorods–nanoflowers	26–29	29.8	88.4
		35–37.5	31.1	91.2
		40.5–43	30	90.2
		53.5–56	25.2	86
b.	Mixed-phase TiO_2 nanostructures	24–27 (A)	18.9	85.2
		27–29 (R)	28.2	76.5
		37–39 (A–R)	20.3	72.5
		47–50 (A)	19.5	86.6
		53.5–55 (A–R)	26.2	75.7
		55–56 (A–R)	39.4	73.5
		61.5–64 (A–R)	19.5	82.9

The rutile and rutile–anatase phases of TiO_2 nanorods–nanoflowers and mixed-phase TiO_2 nanostructures were also confirmed by XRD analysis. The XRD patterns of both samples are presented in Fig. 5. Fig. 5(a) shows 15 peaks, which confirmed that the as-grown TiO_2 nanorods–nanoflowers were in rutile phase. The most intense peak observed at 27.83° represents a plane [110], which suggested that the synthesised TiO_2 nanorods–nanoflowers were grown along that direction. The plane [110] of rutile phase is the most thermodynamically stable; thus, its growth rate is faster than those of other planes [57]. Two intense peaks were located at 36.49° and 41.75°, which represented planes [101] and [111], respectively. The last intense peak observed at 55.07°, represented plane [211] (PDF No.01-071-4809). The high peak intensities indicated that the synthesised film possesses a strong crystallinity. The crystallite percentage of TiO_2 nanorods–nanoflowers film was approximately 83.8%, with the average crystallite size of 25–31 nm. The detailed crystallite size and its percentage for selected peaks are presented in Table 2. The four intense peaks showed high crystallinity of more than 85%, which verified the good quality of the synthesised TiO_2 nanorods–nanoflowers film.

Additional peaks representing anatase phase were observed when TiO_2 nanoparticles were applied on top of TiO_2 nanorods–nanoflowers, as shown in Fig. 5(b). The most intense peak of anatase phase was shown at 25.65°, and it represented plane [101]. Another intense peak was observed at 48.38°, which represented plane [200] (PDF No.01-075-1537). The intense peak of TiO_2 nanorods–nanoflowers film at 27.83° decreases when TiO_2 nanoparticles were applied (Fig. 5(b)). Crystallinity calculation also revealed that the fabricated mixed-phase TiO_2 nanostructures showed only 77.7% crystallite percentage. This result was attributed to the high porosity of TiO_2 nanoparticles morphology, as shown in the FESEM image. According to Fig. 5(b) and Table 2, the crystallite size of the pure anatase phase was ~20 nm, but the peaks of the mixed-phase one were larger at approximately 39 nm. Crystallite calculation also indicated that the mixed-phase TiO_2 nanostructures contained 74.1% anatase and 25.9% of rutile phase. This result confirmed the FESEM images that showed ~76% anatase thickness compared with that of the rutile one.

The measured resistivities of fabricated GO and rGO CE thin films shown in Fig. 6 were 3.13, 3.23 and 3.25 Ωcm for TC14-rGO, TC14-GO and SDS-rGO, respectively. The high resistivity of TC14-GO and SDS-rGO may have resulted from the higher presence of oxygen functional groups than that of TC14-rGO. The oxygen functional groups may prevent the electron movement due to the small electron-conductivity [69]. The slightly lower resistivity of TC14-GO than that of SDS-rGO indicated that TC14 can effectively stabilise the graphitic sheets, which increases the GO sheet dispersion during exfoliation [58]. The almost similar resistivity value of TC14-GO and SDS-rGO samples suggested the similar η value and performance of the DSSCs device. The lowest resistivity value of TC14-rGO confirmed the successful reduction process for reducing oxygen

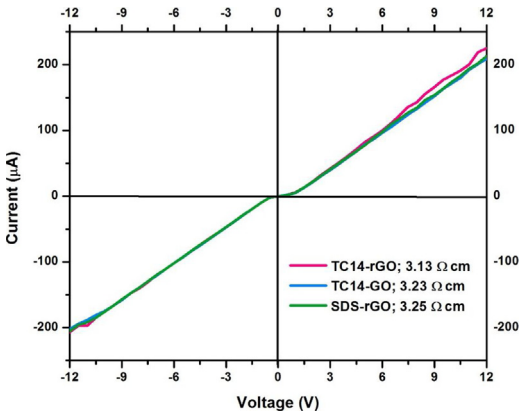

Fig. 6. I–V measurement of fabricated GO and rGO CE thin films.

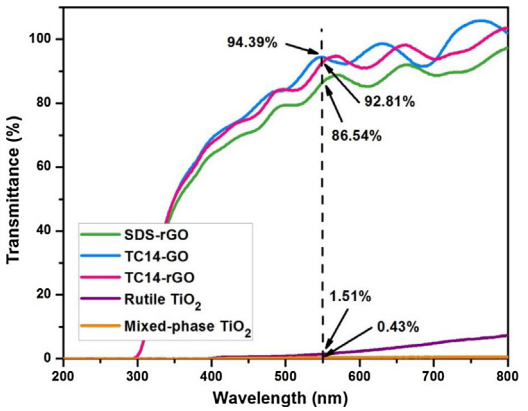

Fig. 7. UV–vis patterns of fabricated photoanode and CE thin films.

functional groups and partially restoring the π−π conjugated structure, which consequently increases the conductivity of the film [69].

The transmittance values of GO and rGO CE thin films were determined at 550 nm wavelength [11]. Fig. 7 shows that SDS-rGO exhibited the lowest transmittance, which was probably due to its thicker layer than that of TC14-rGO. This result also verified the low efficiency of SDS in stabilising the rGO solution. The SDS-rGO sheets restacked and agglomerated due to the low solubility caused by single-tail SDS; such solubility prevents the light movement, thereby reducing the transmittance value [58]. On the contrary, TC14-GO and TC14-rGO showed high solubility due to triple-tail TC14, which was supported with the high transmittance values of 94.39% and 92.81%, respectively. These findings confirmed the effectiveness of TC14 in the dispersion and stabilisation of GO sheets in the solution form. The transmittance for photoanode was considerably low, that is, 1.51% of rutile TiO_2 nanorods–nanoflowers, and decreased to 0.43% for mixed-phase TiO_2 nanostructures. This low value may be due to the uniform and dense as-grown TiO_2 film. The optical band gap (E_g) values for both photoanode and CE films were determined using Tauc plot, as shown in Fig. 8. The E_g photoanode films showed a slight difference between rutile TiO_2 nanorods–nanoflowers and mixed-phase TiO_2 nanostructures, as shown in Fig. 8(a). The rutile TiO_2 nanorods–nanoflowers exhibited 3.00 eV, which is similar to that in [45], and the mixed-phase TiO_2 nanostructures displayed 2.95 eV. The low E_g value indicated that the mixed-phase film performed better in transferring electrons than that of the pure phase film. Consequently, fast electron transfer from excited electron on the TiO_2 nanoparticles was achieved, which increased the photovoltaic performance of the film. The SDS-rGO and TC14-GO CE thin films showed the same E_g value of 4.09 eV, as shown in Fig. 8(b) and (c). The slightly low E_g value of TC14-rGO (4.07 eV) suggested an excellent electron transfer process and that it can be applied as a CE for DSSCs application (Fig. 8(d)). These results were also validated by the I–V measurement results.

The solar simulator measurement results of fabricated DSSCs are plotted as short current density–voltage (J_{SC}–V) curves in Fig. 9. TC14-rGO exhibited the highest efficiency (0.0266%) among samples (0.0139% and 0.0116% for TC14-GO and SDS-rGO, respectively). The inset shown in Fig. 9 revealed a slightly increased η of TC14-GO compared with that of SDS-rGO. This result confirmed the effectiveness of triple-tail TC14 surfactant in the GO layer stabilisation, even with a lower J_{SC} value than that of SDS-rGO. This result was attributed to the high number of oxygen functional groups in the TC14-GO sample. The successful reduction process conducted on TC14-GO confirmed the higher J_{SC} value of TC14-rGO (0.222 mA/cm^2) than

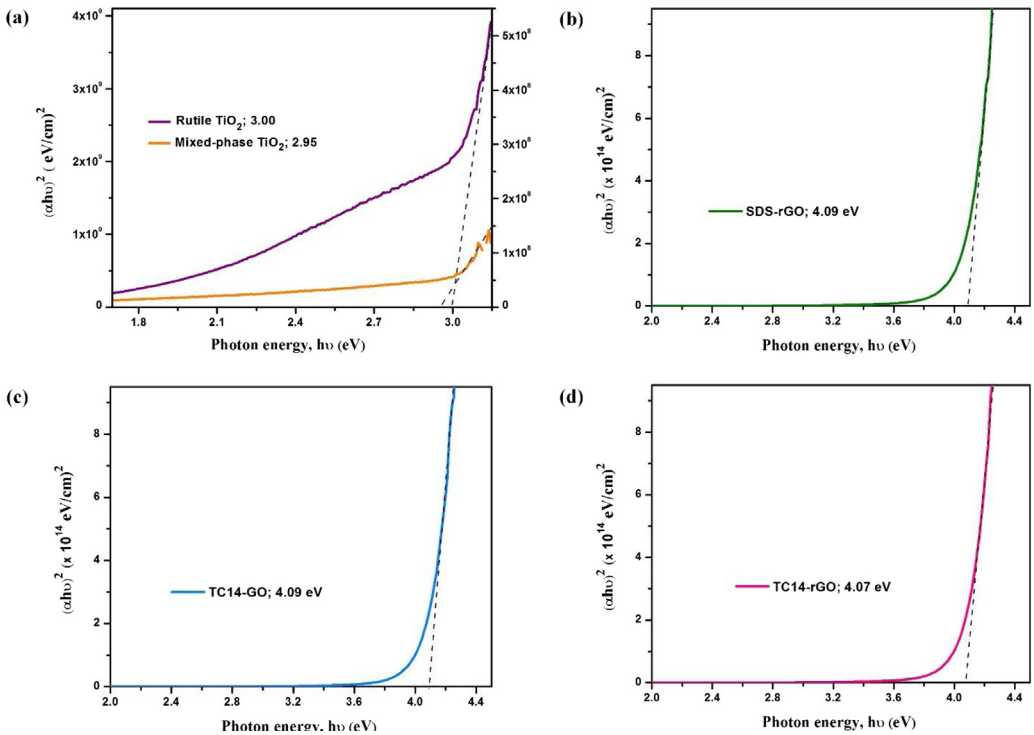

Fig. 8. Optical band gap (E_g) measurement of (a) rutile TiO_2 nanorod–nanoflower and mixed-phase TiO_2 nanostructure, (b) SDS-rGO, (c) TC14-GO and (d) TC14-rGO CE thin films.

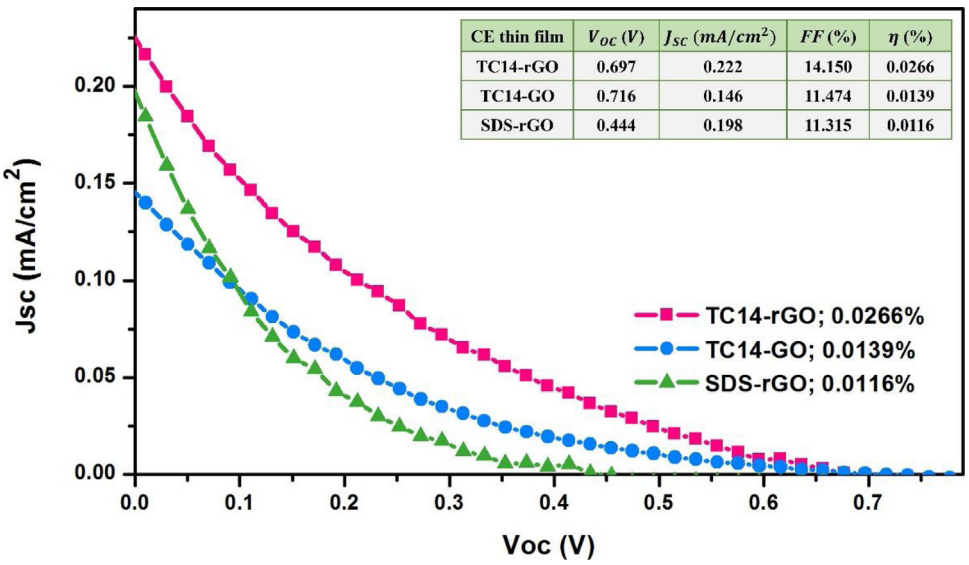

Fig. 9. Solar simulator measurement of DSSCs based on mixed-phase TiO_2 nanostructures as photoanode and GO and rGO as CE thin films.

those of TC14-GO (0.146 mA/cm^2) and SDS-rGO (0.198 mA/cm^2). The high J_{SC} value was also determined by the morphology of CE film. When the collected electrons in the photoanode moved to the CE film, the electrons should move quickly to the CE interface and complete the reduction process in the electrolytes. High catalytic activity of CE film was achieved with the fast reduction process, which resulted in a high η value. The high conductivity of TC14-rGO due to the lowest resistivity helped the electron moved faster through the film and reached CE interface. The high-bridging system of TC14-rGO to the FTO substrate also supports the fast electron movement and decreases the recombination rate and interfacial resistance [28]. This result, which was verified by the low E_g value of TC14-rGO, also verified the stable rGO sheets assisted with TC14,

which improved the electrolyte diffusibility. The large surface area of TC14-rGO increased the number of catalytically active sites of films.

V_{OC} value depends on the components of the entire DSSCs [6]. Given that the photoanode film was fixed by using mixed-phase TiO_2 nanostructures for all samples, changes in V_{OC} value were significantly affected with the different types of GO and rGO materials to fabricate CE thin films. This result confirmed that the GO and rGO films assisted with triple-tail TC14 surfactant were potentially applicable as CEs for DSSCs application due to their V_{OC} value that was highly similar to that of SDS-rGO. The lowest V_{OC} value of rGO film assisted with single-tail SDS surfactant confirmed low effectiveness in terms of GO stabilisation, which affected the electrical properties of the fabricated film. In addition, the higher fill factor (FF) values of TC14-rGO (14.150) than that of SDS-rGO (11.315) supported the high η value. This result was due to the low resistivity and E_g value of TC14-rGO, which enhanced the electron transfer and increased the FF value.

Furthermore, the thick TiO_2 nanoparticles, as the second layer of photoanode film, adsorbed a large amount of dye because of its large surface area and high porosity, as revealed by the FESEM and XRD analysis. This characteristic, which affects the amount of J_{SC}, becomes an important factor in electron excitation. The TiO_2 nanoflowers helped the TiO_2 nanoparticles stick to the photoanode bottom layer without gaps. The utilisation of TTIP in the preparation of TiO_2 paste allowed the close connection of particles with one another, thereby making the excited electrons moved freely through them. The morphology of TiO_2 nanorods that were in the perpendicular direction of FTO caused the electrons to move fast and directly go to the substrate. The dense TiO_2 nanorods also provided an advantage in avoiding electron saturation in the boundary of nanorods and nanoparticles.

4. Conclusion

GO and rGO CE thin films prepared by electrochemical exfoliation and subsequent chemical reduction process and spraying deposition method were investigated in terms of their DSSCs performance. The CE thin film based on triple-tail surfactant (TC14-rGO) performs better than that of the CE thin film based on single-tail surfactant (SDS-rGO). FESEM, HRTEM, micro-Raman and I–V measurement confirmed the improved result of TC14-rGO, which displays the thinnest and fewest layers (~2–4 layers) and the lowest resistivity (3.13 Ωcm). This surfactant also exhibits a high transmittance of 92.81% with 4.07 eV band gap value. Approximately 0.0266% efficiency of DSSCs is obtained when TC14-rGO is assembled with mixed-phase TiO_2 nanostructures synthesised by hydrothermal growth and squeegee method. This efficiency is two times higher than that of SDS-rGO, thereby confirming the effectiveness of TC14 surfactant in the dispersion and stabilisation of GO solution. This result can be used to decrease the Pt loading in the CE fabrication. However, the fabrication of photoanode and CE should be optimised to achieve high efficiency.

Acknowledgment

The authors gratefully acknowledge the financial support provided by the TWAS-COMSTECH Joint Research Grant (Grant code: 2017-0001-102-11) and Fundamental Research Grant Scheme (Grant code: 2015-0154-102-02).

References

[1] M. Grätzel, Nature 414 (2001) 338–344.
[2] D.-D. Qin, Y.-P. Bi, X.-J. Feng, W. Wang, G.D. Barber, T. Wang, Y-M, X.-Q. Song, T.E. Lu, Mallouk, Chem. Mater. 27 (2015) 4180–4183.
[3] S. Mathew, A. Yella, P. Gao, R. H-Baker, B.F.E. Cuchod, N. A-Astani, I. Tavernelli, U. Rothlisberger, Md.K. Naxeeruddin, M. Grätzel, Nat. Chem. 6 (2014) 242–247.
[4] U. Mehmood, Z. Malaibari, F.A. Rabani, A. Ur Rehman, A.H.A. Ahmad, M.A. Atieh, M.S. Kamal, Electrochim. Acta 203 (2016) 162–170.
[5] J. Zhao, J. Wu, M. Zheng, J. Huo, Y. Tu, Electrochim. Acta 156 (2015) 261–266, http://dx.doi.org/10.1016/j.electacta.2015.01.045.
[6] M.Y. Song, K.N. Chaudhari, J. Park, D.-S. Yang, J.H. Kim, M.-S. Kim, K. Lim, J. Ko, J.-S. Yu, Appl. Energy 100 (2012) 132–137.
[7] R. Cruz, D.A.P. Tanaka, A. Mendes, Sol. Energy 86 (2012) 716–724.
[8] Z.Y. Li, M.S. Akhtar, J.H. Kuk, B.-S. Kong, O.-B. Yang, Mater. Lett. 86 (2012) 96–99.
[9] L. Kavan, J.-H. Yu, M. Grätzel, Nano Lett. 11 (2011) 5501–5506.
[10] L. Kavan, J.-H. Yu, M.K. Nazeeruddin, M. Grätzel, J. Am. Chem. Soc. 5 (11) (2011) 9171–9178.
[11] C.-M. Gee, C.-C. Tseng, F.-Y. Wu, H.-P. Chang, L.-J. Li, Y.-P. Hsieh, C.T. Lin, J.-C. Chen, Displays 34 (2013) 315–319.
[12] Y. Pan, Z. Hou, H. Yang, Y.-N. Liu, Mater. Sci. Semicond. Process. 40 (2015) 176–182.
[13] Y.-P. Zhang, J.-J. Xu, Z.-H. Sun, C.Z. Li, C.-X. Pan, Prog. Nat. Sci. Mater. Int. 21 (2011) 467–471.
[14] L.-J. Wang, L. Lei, J. Yu, Y. Wu, H. He, X. Ouyang, X. Zhao, Y.-C. Yen, L.J. Lee, Carbon (2014) 294–301.
[15] S. Mikhailov, Physics and applications of graphene – experiments, in: InTech:Croatia, 2011.
[16] J.H. Kang, T. Kim, J. Choi, J. Park, Y.S. Kim, M.S. Chang, H. Jung, K. Park, S.J. Yang, C.R. Park, Chem. Mater. (2015), http://dx.doi.org/10.1021/acs.chemmater.5b03700.
[17] T.-T. Wu, J.-M. Ting, Surf. Coat. Technol. 231 (2013) 487–491.
[18] J. Kim, L.J. Cote, F. Kim, W. Yuan, K.R. Shull, J. Huang, J. Am. Chem. Soc. 132 (2010) 8180–8186.
[19] A. Ambrosi, M. Pumera, Chem. Eur. J. 22 (2016) 153–159.
[20] P. Yu, S.E. Lowe, G.P. Simon, Y.L. Zhong, Curr. Opin. Colloid Interface. Sci. (2015), http://dx.doi.org/10.1016/j.cocis.2015.10.007.
[21] K. Parvez, R. Li, S.R. Puniredd, Y. Hernandez, F. Hinkel, S. Wang, X. Feng, K. Müllen, ACS Nano 7 (2013) 3598–3606, http://dx.doi.org/10.1021/nn400576v.
[22] J. Liu, C.K. Poh, D. Zham, L. Lai, S.H. Lim, L. Wang, X. Liu, N.G. Sahoo, C. Li, Z. Shen, J. Lin, Nano Energy (2012), http://dx.doi.org/10.1016/j.nanoen.2012.11.003.
[23] A. Mohamed, A.K. Anas, A.B. Suriani, A.A. Azira, M. Sagisaka, P. Brown, J. Eastoe, A. Kamari, N. Hashim, I.M.D. Isa, Colloid. Polym. Sci. 292 (2014) 3013–3023.

[24] A. Mohamed, A.K. Anas, A.B. Suriani, T. Ardyani, W.M.W. Zin, S. Ibrahim, M. Sagisaka, P. Brown, J. Eastoe, J. Colloid Interface Sci. 455 (2015) 179–187.
[25] A. Mohamed, T. Ardyani, A.B. Suriani, P. Brown, M. Hollamby, M. Sagisaka, J. Eastoe, Adv. Colloid Interface Sci. 230 (2016) 54–69.
[26] A.B. Suriani, M.D. Nurhafizah, A. Mohamed, I. Zainol, A.K. Masrom, Mater. Lett. 161 (2015) 665–668.
[27] A.B. Suriani, M.D. Nurhafizah, A. Mohamed, A.K. Masrom, V. Sahajwalla, R.K. Joshi, Mater. Des. 99 (2016) 174–181.
[28] A.B. Suriani, M.D. Nurhafizah, A. Mohamed, A.K. Masrom, M.H. Mamat, M.F. Malek, M.K. Ahmad, M.S. Rosmi, M. Tanemura, J. Mater. Sci. 52 (2017) 6611–6622.
[29] C.K. Chua, M. Pumera, Chem. Soc. Rev. 43 (2014) 291–312.
[30] V.H. Pham, T.V. Cuong, S.H. Hur, E.W. Shin, J.S. Kim, J.S. Chung, E.J. Kim, Carbon 48 (2010) 1945–1951.
[31] M. Beidaghi, Z. Wang, L. Gu, C. Wang, J. Solid State Electrochem. 16 (2012) 3341–3348.
[32] C. Sima, C. Grigoriu, S. Antohe, Thin Solid Films 519 (2010) 595–597.
[33] C.Y. Jiang, X.W. Sun, G.Q. Lo, D.L. Kwong, J.X. Wang, Appl. Phys. Lett. 90 (2007) 263501, http://dx.doi.org/10.1063/1.2751588.
[34] E. Ramasamy, J. Lee, J. Phys. Chem. 114 (2014) 22032–22037.
[35] J. Gong, J. Liang, K. Sumathy, Renew. Sustain. Energy Rev. 16 (C) (2012) 5848–5860.
[36] C.W. Kim, S.P. Suh, M.J. Choi, Y.S. Kang, Y.S. Kang, J. Mater. Chem. A 1 (2013) 11820.
[37] M.K. Ahmad, S.M. Mokhtar, C.F. Soon, N. Nafarizal, A.B. Suriani, A. Mohamed, M.H. Mamat, M.F. Malek, M. Shimomura, K. Murakami, J. Mater. Sci.: Mater. Electron. 27 (2016) 7920–7926.
[38] M.K. Ahmad, V.M. Mohan, K. Murakami, J. Sol.-Gel Sci. Technol. 73 (2015) 655–659.
[39] D. Zhang, T. Yoshida, T. Oekermann, K. Furuta, H. Minoura, Adv. Funct. Mater. 16 (2006) 1228–1234.
[40] M.K. Ahmad, C.F. Soon, N. Nafarizal, A.B. Suriani, A. Mohamed, M.H. Mamat, M.F. Malek, M. Shimomura, K. Murakami, Optik 127 (2016) 1063–1068.
[41] F.I.M. Fazli, M.K. Ahmad, C.F. Soon, N. Nafarizal, A.B. Suriani, A. Mohamed, M.H. Mamat, M.F. Malek, M. Shimomura, K. Murakami, Optik 140 (2017) 4076–4079.
[42] D.-W. Han, J.-H. Heo, -J. Kwak, C.-H. Han, Y.-M. Sung, J. Electr. Eng. Technol. 4 (1) (2009) 93–97.
[43] Y. Fukai, Y. Kondo, S. Mori, E. Suzuki, Electrochem. Commun. 9 (7) (2007) 1439–1443.
[44] C. Bauer, G. Boschloo, E. Mukhtar, A. Hagfeldt, Int. J. Photoenergy 4 (1) (2002) 17–20.
[45] J. Lei, H. Li, J. Zhang, M. Anpo, Mixed-Phase TiO_2 Nanomaterials as Efficient Photocatalysts, in: H. Ünlü, N. Horing, J. Dabrowski (Eds.), Low-Dimensional and Nanostructured Materials and Devices. NanoScience and Technology, Springer, Cham, 2016.
[46] V. Tamilselvan, D. Yuvaraj, R.R. Kumar, K.N. Rao, Appl. Surf. Sci. 258 (2012) 4283–4287.
[47] Y.J. Hwang, C. Hahn, B. Liu, P. Yang, Am. Chem. Soc. 6 (6) (2012) 5060–5069.
[48] S.I. In, K.P. Almtoft, H. Lee, I.H. Andersen, D.-D. Qin, N. Bao, C.A. Grimes, Bull. Korean Chem. Soc. 33 (6) (2012) 1989–1992.
[49] J.Z. Chen, Y.C. Yan, K.J. Lin, J. Chin. Chem. Soc. 57 (2010) 1180–1184.
[50] Z. Liu, C. Liu, J. Ya, E. Lei, Renew. Energ. 36 (2011) 1177–1181.
[51] S.C. Yang, D.J. Yang, J. Kim, J.M. Hong, H.G. Kim, I.D. Kim, H. Lee, Adv. Mater. 20 (2008) 1059–1064.
[52] Z.-S. Wang, M. Yanagida, K. Sayama, H. Sugihara, Chem. Mater. 18 (2006) 2912–2916.
[53] Y. Chiba, A. Islam, R. Komiya, N. Koide, L. Han, J. Appl. Phys. Lett. 88 (2006) 223505, http://dx.doi.org/10.1063/1.2208920.
[54] J.M. Kroon, N.J. Bakker, H.J.P. Smit, P. Liska, K.R. Thampi, P. Wang, S.M. Zakeeruddin, M. Grätzel, A. Hinsch, S. Hore, U. Würfel, R. Sastrawan, J.R. Durrant, E. Palomares, H. Pettersson, T. Gruszecki, J. Walter, K. Skupien, G.E. Tulloch, Prog. Photovolt: Res. Appl. 15 (2007) 1–18.
[55] Z. Liu, X. Zhang, S. Nishimoto, M. Jin, D.A. Tryk, T. Murakami, A. Fujishima, Langmuir 23 (2007) 10916–10919.
[56] Q. Zhu, J. Qian, H. Pan, L. Tu, X. Zhou, Nanotechnol. 22 (2011), 395703 (9pp).
[57] W. Zhou, X. Liu, J. Cui, D. Liu, J. Li, H. Jiang, J. Wang, H. Liu, Cryst. Eng. Comm. 13 (2011) 4557–4563.
[58] A.B. Suriani, M.D. Nurhafizah, A. Mohamed, M.H. Mamat, M.F. Malek, M.K. Ahmad, A. Pandikumar, N.M. Huang, Optics 139 (2017) 291–298.
[59] U. Balachandran, N.G. Eror, J. Solid State Chem. 42 (1982) 276–282.
[60] M.M. Yusoff, M.H. Mamat, M.F. Malek, A.B. Suriani, A. Mohamed, M.K. Ahmad, S.A.H. Alrokayan, H.A. Khan, M. Rusop, Mater. Lett. 164 (2016) 294–298.
[61] C. Aprile, L. Maretti, M. Alvaro, J.C. Scaiano, H. Garcia, Dalton Trans. 40 (2008) 5465–5470.
[62] R.J. Meier, Chem. Soc. Rev. 34 (2005) 743–752.
[63] Z. Luo, A.S. Poyraz, C.-H. Kuo, R. Miao, Y. Meng, S.-Y. Chen, T. Jiang, C. Wenos, S.L. Suib, Chem. Mater. 27 (1) (2014) 6–17.
[64] S.M. Mokhtar, M.K. Ahmad, C.F. Soon, N. Nafarizal, A.B. Faridah, A.B. Suriani, M.H. Mamat, M. Shimomura, K. Murakami, Optik 154 (2018) 510–515.
[65] M.S. Dresselhaus, A. Jorio, M. Hofmann, G. Dresselhaus, R. Saito, Nano Lett. 10 (2010) 751–758.
[66] M.D. Nurhafizah, A.B. Suriani, S. Alfarisa, A. Mohamed, M.D. Ilyas, A. Kamari, N. Hashim, A.A. Aziz, M.R. Mahmood, Adv. Mater. Res. 1109 (2015) 55–59.
[67] K.H. Lee, B. Lee, S.J. Hwang, J.U. Lee, H. Cheong, O.S. Kwon, K. Shin, N.H. Hur, Carbon 69 (2014) 327–335.
[68] H. Wang, Y. Wang, X. Cao, M. Feng, G. Lan, J. Raman Spectrosc. 40 (2009) 1791–1796.
[69] C. Hu, R. Zhou, C. Fan, X. Zhou, Micro Nano Lett. 11 (4) (2016) 215–220.